Temporal and spatial valley dynamics in two-dimensional semiconductors probed via Kerr rotation

Citation: Huang, Jiani; Hoang, Thang B.; Ming, Tian; Kong, Jing and Mikkelsen, Maiken H. "Temporal and spatial valley dynamics in two-dimensional semiconductors probed via Kerr rotation." Physical Review B 95, no. 075428 (February 2017): 1-7 ©2017 American Physical Society

As Published: http://dx.doi.org/10.1103/PhysRevB.95.075428

Publisher: American Physical Society

Persistent URL: http://hdl.handle.net/1721.1/109187

Version: Final published version: final published article, as it appeared in a journal, conference proceedings, or other formally published context

Temporal and spatial valley dynamics in two-dimensional semiconductors probed via Kerr rotation

Jiani Huang,[1] Thang B. Hoang,[1,*] Tian Ming,[2] Jing Kong,[2] and Maiken H. Mikkelsen[1,3]
[1]*Department of Physics, Duke University, Durham, North Carolina 27708, USA*
[2]*Department of Electrical Engineering and Computer Science, Massachusetts Institute of Technology, Cambridge, Massachusetts 02139, USA*
[3]*Department of Electrical and Computer Engineering, Duke University, Durham, North Carolina 27708, USA*
(Received 28 April 2016; revised manuscript received 3 January 2017; published 24 February 2017)

Monolayer transition metal dichalcogenides (TMDCs) offer a tantalizing platform for control of both spin and valley degrees of freedom, which may enable future optoelectronic devices with enhanced and novel functionalities. Here, we investigate the valley dynamics of two prototypical members of TMDCs, namely MoS_2 and WSe_2, using time-resolved Kerr rotation (TRKR) at temperatures from 10 K to 300 K. This pump-probe technique enables sub-picosecond temporal resolution, providing insight into ultrafast valley dynamics, which is inaccessible by polarized and time-resolved photoluminescence spectroscopy. Bi-exponential decay dynamics were observed for both materials at low temperatures, and the fast decay component indicated a rapid exciton valley depolarization time (<10 ps) due to strong Coulomb exchange interactions between the K valleys. However, the slow decay components (several tens of picoseconds) were attributed to different origins in the two materials, which were further elucidated by temperature-dependent TRKR measurements. Moreover, the spatial dependence of the TRKR intensity across MoS_2 monolayer flakes indicated a weaker valley polarization near the edges, which is likely associated with quenched excitons near the grain boundaries or a disordered edge region in chemical vapor deposition–grown monolayers. These temporal and spatial TRKR measurements reveal insight into the complex dynamics of valley excitonic states, which will be critical for valleytronic applications of monolayer TMDCs.

DOI: 10.1103/PhysRevB.95.075428

Monolayer transition metal dichalcogenides (TMDCs), such as MoS_2 and WSe_2, are two-dimensional (2D) semiconductors with fascinating electronic and optical properties [1]. Compared with few-layer TMDCs, a direct bandgap in monolayer TMDCs at the $\pm K$ points near the edges of the first Brillouin zone results in greatly enhanced photoluminescence (PL) quantum yield [2], making them ideal candidates for optoelectronic applications. Additionally, the lack of inversion symmetry together with a strong spin-orbit coupling lead to a large valence band splitting in monolayer TMDCs [3]. This splitting lifts the spin degeneracy of both electron and hole states in the $\pm K$ valleys, enabling the excitation of carriers with various combinations of spin and valley indices. Thus, the optical selection rules allow both spin and valley states in monolayer TMDCs to be coupled to σ^+ or σ^- polarized light, making them a promising nanoscale system for future spintronic and valleytronic applications.

Acting as the key operation element for valleytronic devices, the manipulation of valley excitonic states has been demonstrated by a variety of experimental methods to date [4–7]. However, fundamental timescales in monolayer TMDCs are still not well understood, such as exciton radiative lifetime, photocarrier recombination time, and valley relaxation time. Some of the published time-resolved and pump-probe measurements for the four most commonly studied monolayer TMDCs are listed in Supplemental Material Table S1. [24]. Time-resolved PL spectroscopy has shown fast exciton decay times of 2–5 ps but was limited by the instrument response time [8–12]. Recent pump-probe transient absorption measurements observed an ultrafast exciton lifetime of 1–2 ps [13–16], which was attributed to ultrafast radiative recombination of excitons [13], fast defect capture [14], carrier-carrier scattering [15], or fast electron valley depolarization [16]. Additionally, most time-resolved experiments displayed bi-exponential or tri-exponential decay dynamics, and the slower decay components of several tens of picoseconds were attributed to different origins such as trion emission decay [9], slow defect capture [14], carrier-phonon scattering [15], or hole valley relaxation [16]. Several more recent reports observed nanosecond decay [17–19]; however, this was attributed to different origins, including a polarization of resident carriers, electron spin relaxation, or hole valley depolarization. In these studies, a significant dependence was also observed upon specific experimental conditions and the spatial locations that were probed within single flakes. Therefore, further investigation of these timescales is essential to understand and utilize the valley properties in monolayer TMDCs.

In this work, we investigated the valley dynamics of monolayer TMDCs using time-resolved Kerr rotation (TRKR) microscopy, which provides a sensitive and direct probe of the spin and valley polarization and has been widely used to investigate spin dynamics in conventional semiconductors [20–22]. For monolayer TMDCs, TRKR measurements allow us to probe the valley states of both photo-excited and resident carriers polarized by a pump pulse with σ^+ or σ^- polarization, at any time as given by the delay between the pump and probe pulses. At low temperature, we observed bi-exponential decay dynamics for both MoS_2 and WSe_2 monolayers when their excitation energies were tuned slightly above the A exciton resonance to achieve the maximum Kerr rotation intensity. The fast decay components were observed to be less than 10 ps, indicating rapid exciton valley depolarization due to strong long-range Coulomb exchange interactions between the $\pm K$ valleys. The slow decay components, however, have different

*Present address: Department of Physics and Materials Science, The University of Memphis, Memphis Tennessee 38152, USA.

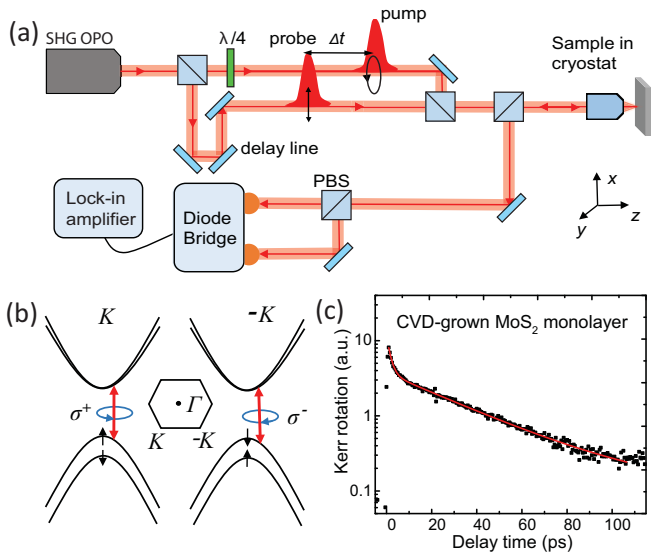

FIG. 1. TRKR measurements of valley dynamics. (a) Schematic diagram of the experimental setup. (SHG OPO: second-harmonic generation of optical parametric oscillator; PBS: polarizing beam-splitter; $\lambda/4$: quarter-wave plate.) (b) Diagram of the valley-dependent optical selection rules for the interband transitions. (c) Valley dynamics measured by TRKR for a CVD-grown MoS_2 monolayer at $T = 10$ K with a laser excitation energy of 1.93 eV. The solid line shows a bi-exponential fit to the experimental data.

origins in the two materials. The trion depolarization accounts for the slow decay component in MoS_2, whereas the slow decay component in WSe_2 is likely associated with defect-related localized states. The different underlying mechanisms for the slow decay components in the two materials were further explored by temperature-dependent TRKR measurements from 10 K to 300 K. Additionally, we investigated the spatial dependence of the Kerr rotation intensity at a fixed pump-probe delay time across MoS_2 monolayer flakes at both $T = 10$ K and room temperature, which is critical for understanding valley dynamics of excitonic states over large areas.

The samples used in the experiments are MoS_2 monolayers fabricated by chemical vapor deposition (CVD) as described in Ref. [23], and WSe_2 monolayers from micromechanical cleavage of bulk crystals (optical and atomic force microscopy characterization is shown in Supplemental Material Fig. S1 [24]). In the experimental setup shown in Fig. 1(a), we used energy degenerate pump and probe pulses from a tunable frequency-doubled optical parametric oscillator synchronously pumped by a Ti^{3+}: sapphire laser (~150 fs pulse duration, 80 MHz repetition rate) for the TRKR measurements. A nonpolarizing beam-splitter was used to divide the laser into two different paths, namely, the pump and probe beams. For circularly polarized excitation, the pump beam passed through a linear polarizer followed by a quarter-wave plate. For the probe beam, a Glan-Thompson polarizer was used to create the linear polarization. To control the time delay between the arrival of the pump and probe pulses, the probe beam passed through a mechanical delay line consisting of a retro-reflector mirror on a 1 m linear ball-bearing slide stage. A computer-controlled stepper motor drove the stage through a belt-gear attachment. Finally, the two beams were spatially overlapped and focused on the sample via a 50×, 0.65 numerical aperture microscope objective with an ~1.5-μm-diameter spot size. The sample was placed in a helium-flow magneto-optical cryostat, which was mounted on a 2D translation stage, allowing for fine adjustments along the x and y directions. In the collection path, a spatial filter, consisting of a lens pair and a pinhole, was used to block the pump beam and let the probe beam pass through. The probe beam went through a half-wave plate followed by a 50:50 polarizing beam-splitter, which separated the horizontally and vertically polarized components. These two beams were then focused onto the two diodes of a balanced photodiode bridge (Thorlabs, PDB 210A), where the difference signal is proportional to the Kerr rotation angle. Because this angle is typically very small (approximately milliradians), a pre-amplifier and lock-in detection were used to isolate the desired signal from the background noise.

Due to the valley-dependent optical selection rules for the interband transitions shown in Fig. 1(b), the helicity of the circularly polarized pump is well coupled to the valley index and selectively excites electron-hole pairs in one of the K valleys. This creates an imbalance between the populations in the two valleys and results in a relative shift between the absorption spectra of σ^+ and σ^- polarized light. Because the absorption and index of refraction are linked by the Kramers-Kronig relations, a difference occurs between the refractive indices of σ^+ and σ^- polarized light. This difference is measured through a rotation of the polarization axis of the linearly polarized probe upon reflection off the sample, referred to as the Kerr rotation angle, and it is measured at varying time delays, Δt, between the pump and probe pulses. Therefore, the Kerr rotation angle is linearly proportional to the valley polarization along the direction of the beam propagation and can be expressed as [25–27]:

$$\theta_K = \mathrm{Im}[\gamma(\alpha_+ - \alpha_-)] \quad (1)$$

where θ_K is the induced Kerr rotation angle, γ is a parameter that accounts for the optical properties of the substrate and small sample variations, and $\alpha_+ - \alpha_-$ is the difference between the complex optical response of the σ^+ and σ^- polarized light, which is induced by the imbalance between the populations in the $\pm K$ valleys upon optical excitation. Figure 1(c) shows the valley dynamics of a CVD-grown monolayer MoS_2 sample that was measured using TRKR at a temperature of $T = 10$ K.

To confirm the origin of the Kerr rotation signal in monolayer TMDCs, we first performed TRKR measurements for a CVD-grown MoS_2 monolayer at different excitation energies at a fixed temperature of $T = 10$ K. Figure 2 displays the excitation energy dependence of the valley dynamics for the monolayer MoS_2 when the excitation energy is tuned from 1.84 eV to 2.07 eV. Representative TRKR spectra for five excitation energies are shown in Fig. 2(a), and bi-exponential decay dynamics were observed for all of the measured excitation energies. Moreover, the two extracted decay components (T_{fast} and T_{slow}) from bi-exponential fits to the data were almost independent of the excitation energy between 1.84 eV and 2.07 eV, as shown in Fig. 2(b). A slight variation in the fast decay component is likely because of different valley depolarization times for the A and B excitons. Nevertheless, this

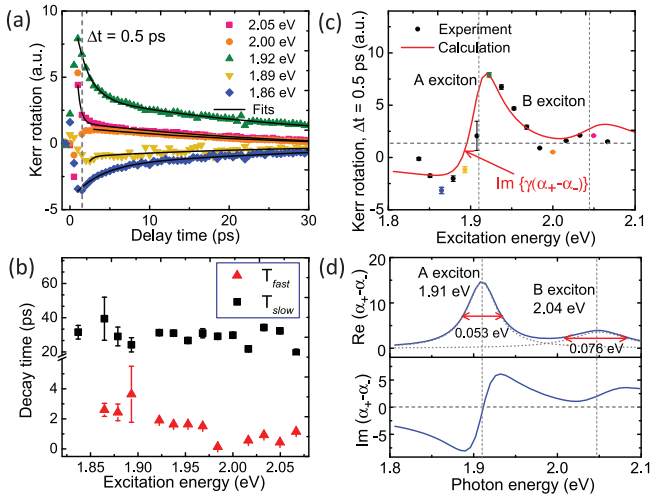

FIG. 2. Excitation energy dependence of valley dynamics of monolayer MoS_2 at $T = 10$ K. (a) Measured Kerr rotation as a function of pump-probe delay time for a range of excitation energies as indicated in the figure. Bi-exponential fits to the data are also shown. (b) The two decay components that were extracted from the bi-exponential fits to the TRKR data as a function of excitation energy. (c) Measured Kerr rotation at a pump-probe delay time of $\Delta t = 0.5$ ps as a function of excitation energy. The solid circles represent experimental data, and the colors correspond to the excitation energies indicated in (a). The prediction from Eq. (1) is shown by the red solid line. (d) The real and imaginary parts of the difference in the complex optical response function $(\alpha_+ - \alpha_-)$ for σ^+ and σ^- polarized light. The imaginary part was calculated from the real part using the Kramers-Kronig relations.

nearly excitation-energy-independent observation indicates that no other valley states such as dark excitons or biexcitons appeared within the measured excitation energies. However, the Kerr rotation intensity at a fixed pump-probe delay time of $\Delta t = 0.5$ ps displayed a strong dependence on the excitation energy, with a pronounced peak at $\sim$1.93 eV, where the excitation energy was close to the A exciton emission energy ($\sim$1.91 eV) as seen in Fig. 2(c). This peak indicates the excitation energy that is observed to generate the largest optically induced valley polarization in monolayer MoS_2. A clear sign reversal of the Kerr rotation intensity was observed at an excitation energy of $\sim$1.9 eV near the A exciton emission energy.

To further elucidate this excitation energy dependence, we consider Eq. (1) again. We assume that the real part of the complex optical response, $\mathrm{Re}(\alpha_+ - \alpha_-)$, is an integrated Lorentz function representing the typical absorption spectrum of monolayer MoS_2. The four parameters as indicated in the top panel of Fig. 2(d) were extracted from our measured absorption spectrum of monolayer MoS_2 with typical A and B exciton absorption peaks at 1.91 eV and 2.04 eV, respectively [28]. Thus, the imaginary part $\mathrm{Im}(\alpha_+ - \alpha_-)$ can be calculated using the well-known Kramers-Kronig relations and is shown in the bottom panel of Fig. 2(d). The parameter γ in Eq. (1) is associated with the optical properties of the substrate, sample geometry, doping level, and other experimental conditions. Here, for simplicity, we assume that γ is independent of the excitation energy for the range of interest and is found to be a complex constant, which is also consistent with a previous report [25]. Based on this, the excitation energy dependence of the TRKR intensity was calculated from Eq. (1) and is shown by the red line in Fig. 2(c) along with the experimental data. As can be seen, the prediction from Eq. (1) reveals a very good agreement with the experimental data. As restricted by our experimental setup, the absorption spectrum of monolayer MoS_2 was obtained from another flake at room temperature, and so the position and linewidth of the excitons were slightly shifted when the sample was cooled down. This is the main reason for the discrepancy between the calculation from Eq. (1) and the experimental data in the vicinity of the B exciton peak. Moreover, a slight deviation at the excitation energy below the A exciton resonance (between 1.8 eV and 1.9 eV) may be due to the excitation energy dependence of the valley polarization, a phenomenon that has been reported for monolayer MoS_2 [4] and WSe_2 [29]. Our observations are consistent with previous polarization-resolved PL measurements that revealed a larger degree of valley polarization for near-resonant than for off-resonant excitation [4,29]. Therefore, from the excitation energy–dependent TRKR measurements, we verified that the observed Kerr rotation signal was primarily originating from the difference between the optical responses of the σ^+ and σ^- polarized light, which is also proportional to the valley polarizations generated by the circularly polarized pump beam. Similar energy-dependent TRKR results should also be expected for the exfoliated monolayer WSe_2 sample, but more resonant peaks and narrower linewidths may be observed, considering the different absorption and emission spectra of monolayer WSe_2 compared to those of monolayer MoS_2.

Next, to explore material variations, we performed TRKR measurements of monolayer MoS_2 and WSe_2, two prototypical members of TMDCs that exhibit strikingly different PL spectra at low temperature, as shown in Fig. 3(a) and 3(c). Based on the above analysis of the excitation energy–dependent TRKR measurements for monolayer MoS_2, we determined that the Kerr rotation intensity is the highest when the excitation energy (1.93 eV) is slightly above the A exciton resonance (1.91 eV). Thus, we chose an excitation energy of 1.75 eV for the following TRKR measurements for monolayer WSe_2, which is slightly above the A exciton resonance (1.73 eV), as can be seen from the PL spectrum in Fig. 3(c). Figure 3(b) and Figure 3(d) display representative valley dynamics that were measured by TRKR on monolayer MoS_2 and WSe_2 respectively, at a temperature of $T = 10$ K. When the pump helicity was switched from σ^+ to σ^- polarization, the TRKR signal was reversed for both samples, as expected from the optical selection rules for the intervalley transitions as shown in Fig. 1(b). We also verified that the applied pump and probe powers were within the linear regime by performing power-dependent TRKR measurements, as shown in Supplemental Material Fig. S2 [24]. For all of the following measurements, the pump and probe powers were kept in the linear regime at 1.5 mW and 0.2 mW, respectively.

Contrary to the single-exponential decay previously observed in monolayer WSe_2 at low temperature [17,30], we observed bi-exponential decay dynamics for both MoS_2 and WSe_2 monolayers. The two decay components that were obtained from fits to the data shown in Fig. 3(b) and 3(d) are 1.6 ± 0.1 ps and 31 ± 2 ps (MoS_2); and 6.7 ± 0.2 ps and 70 ± 6 ps (WSe_2). For monolayer MoS_2, the bi-exponential behavior was

observed from 20 different flakes, as shown in Supplemental Material Fig. S3 [24], displaying only minor variations from sample to sample for both the fast and slow decay components. Therefore, this sample-independent observation is most likely an indication of the intrinsic neutral exciton and trion states rather than other defect-related localized states. Because the TRKR signal is not only affected by the valley polarization of the excitons and trions, but also by the overall exciton density created from optical pumping, an ultrafast radiative decay time arising from both polarized and unpolarized excitons is also expected. This radiative decay time for excitons has been observed to be 1–2 ps in previous pump-probe transient absorption measurements [12–15]. Additionally, a rapid exciton valley depolarization time also on the timescale of several picoseconds has been reported [30], which arises from the strong long-range Coulomb exchange interactions between the nonequivalent K valleys [31,32]. Thus, this fast decay component ($\sim$1.6 ps) in monolayer MoS_2 originates from the neutral exciton valley depolarization with small contributions from the radiative decay of the excitons. For the slow decay time, as previously observed in time-resolved PL measurements [9], the trion emission decays within several tens of picoseconds, and trion polarization is expected to be more stable than neutral exciton polarization, because trions in the $\pm K$ valleys are not coupled to Coulomb exchange interaction. Therefore, even though both excitons and trions coexist during the initial several picoseconds, neutral exciton polarization decays much faster than trion polarization and hence dominates the decay dynamics as a consequence of the intervalley scattering caused by the Coulomb exchange interaction. After a majority of the exciton polarization relaxes, the trion polarization gradually evolves, showing a slower decay time of $\sim$31 ps. We also note that the defect states in the sample may contribute to the slight sample variations in the slow decay time as shown in Supplemental Material Fig. S2 [24].

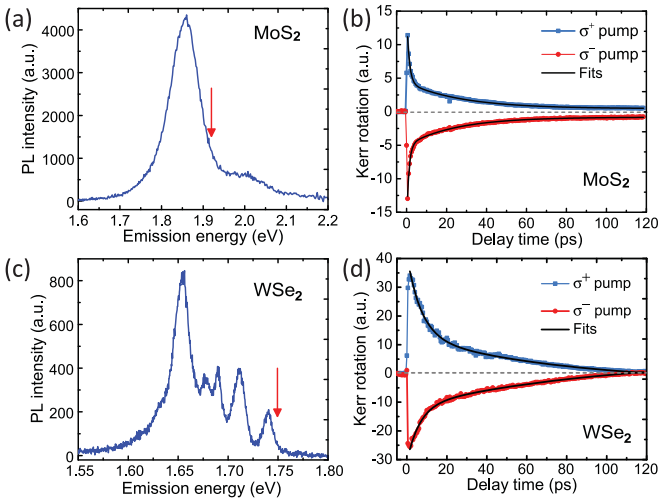

FIG. 3. PL spectra and valley dynamics of MoS_2 and WSe_2 monolayers. (a) PL spectrum of a monolayer MoS_2 measured at $T = 10$ K. (b) TRKR measured for a monolayer MoS_2 at a temperature of $T = 10$ K. An excitation energy of 1.93 eV was used in this experiment as indicated by the arrow in (a). (c) PL spectrum of an exfoliated WSe_2 monolayer flake at $T = 10$ K. (d) TRKR measured for a WSe_2 monolayer flake [exfoliated from the same crystal as the monolayer measured in (c)] at a temperature of $T = 10$ K. An excitation energy of 1.75 eV was used in this experiment as indicated by the arrow in (c). The opposite TRKR signal was observed for σ^+ and σ^- pump polarizations for both monolayer MoS_2 and WSe_2. The solid lines in (b) and (d) are fits to a bi-exponential decay function.

For monolayer WSe_2, the fast decay component of $\sim$6.7 ps is dominated by the neutral exciton depolarization, similar to monolayer MoS_2, despite the coexistence of both exciton and trion polarizations during the initial several picoseconds. However, the slow decay component of 70 ps for monolayer WSe_2 has a different origin than for monolayer MoS_2. One possible explanation could be related to the existence of an intervalley dark exciton state [33–35], where a hole in the valence band of the $+K$ valley is radiatively recombined with an electron in the conduction band of the $-K$ valley upon optical excitation. However, as has been observed in previous PL measurements [33], an important indication of the existence of dark excitons is that the PL intensity increases as the temperature increases, which is the opposite trend to our previous observation [29]. Additionally, the decay time of dark excitons is typically several nanoseconds, which is considerably longer than for bright excitons and trions, whereas the observed decay time of 70 ps in our experiment is relatively short. Thus, a more likely explanation is associated with defect-related localized states. Previous polarization-resolved PL measurements have observed a small but finite degree of circular polarization for the localized states [9,29,36]. The origin of this finite valley polarization is not fully understood yet, but one of the possible explanations relates to a partial transfer of the valley polarization from photo-excited electron-hole pairs to the localized carriers, which can be further captured by the defects in the material. This timescale is considerably longer than previously observed by time-resolved PL [8] and pump-probe differential transmission measurements [14].

To further illuminate the valley dynamics in monolayers MoS_2 and WSe_2, we performed TRKR measurements at different temperatures for both materials, as shown in Fig. 4. For MoS_2, no significant variations were observed for the decay components below 30 K. However, for temperatures above 30 K, we observed a clear decrease of the slow decay component down to 12 ps at $T = 125$ K, whereas the fast decay component was observed to be almost unchanged from 10 K to 125 K. Similar temperature-dependent behavior was observed from three different MoS_2 samples [represented by different colors in Fig. 4(b)]. Additionally, the TRKR signal could even be detected at room temperature, and the extracted decay components obtained on another MoS_2 sample at room temperature before it was cooled down [represented by the green symbols in Fig. 4(b)] were consistent with the observed temperature-dependent trend. The observation of the decay components of both excitons and trions at room temperature relates to the large binding energies [37,38] and the large valley polarizations of these quasiparticles of monolayer MoS_2 [8]. The fast trion depolarization time at higher temperatures is due to phonon-related scattering processes, which cause the valley polarization to relax more rapidly. Moreover, the distinct temperature dependencies of the fast and slow decay components reveal a strikingly different coupling strength of exciton-phonon and trion-phonon interactions,

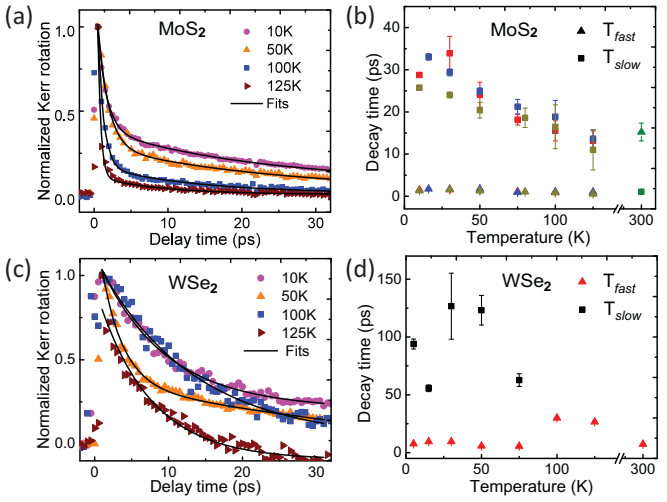

FIG. 4. Temperature dependence of valley dynamics measured by TRKR. (a) The valley dynamics of a monolayer MoS_2 flake at different temperatures. The solid lines are fits to a bi-exponential decay function. (b) The extracted two decay components for MoS_2 as a function of temperature. Different colors represent three different MoS_2 flakes. The green symbols represent the extracted decay components obtained at room temperature for another monolayer flake before the sample was cooled down. (c) The valley dynamics of a monolayer WSe_2 flake at different temperatures. The solid lines are fits to either a bi-exponential or a single-exponential decay function. (d) The extracted two decay components of the same WSe_2 monolayer flake as a function of temperature.

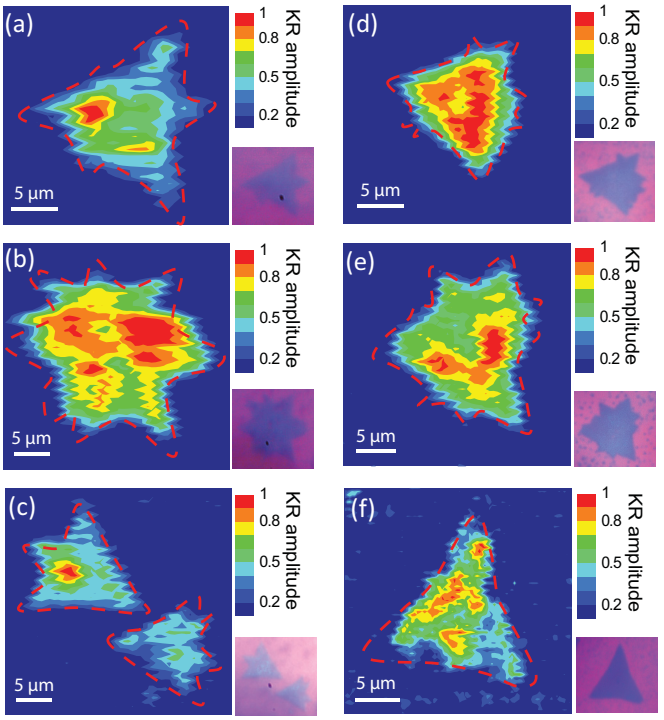

FIG. 5. Spatial distributions of valley dynamics. Two-dimensional maps of TRKR intensity at a fixed pump-probe delay time ($\Delta t = 0.5$ ps) for six monolayer MoS_2 flakes and their corresponding optical microscopy images at (a–c) $T = 10$ K and (d–f) room temperature. The TRKR intensity was normalized for each 2D map. The red dashed line represents the edges of each flake. Laser spot diameter: $\sim 1.5\,\mu$m. Scanning resolution: $0.5\,\mu$m.

but the underlying coupling mechanism still needs further investigation.

For WSe_2, the valley polarization also displayed a bi-exponential decay below 75 K, and the two decay components decreased in a similar fashion to monolayer MoS_2 as the temperature increased. However, for $T \geqslant 100$ K, we observed a clear mono-exponential decay lasting up until room temperature. This transition from bi- to mono-exponential decay may arise from the thermalization of the defect-related localized states: As the temperature increased, carriers were released from the trapped levels and recombined radiatively, leading to increased populations in both exciton and trion states. We also note from our previous temperature-dependent PL measurements that the trion emission peak was much stronger than the exciton emission peak and dominated the PL spectrum in a certain temperature range [29]. Thus, after the defect states vanished at a temperature between 75 K and 100 K, the domination of the trion polarization gives a decay time of $\sim$30 ps at $T = 100$ K and $\sim$25 ps at $T = 125$ K, while the decay time of $\sim$7 ps at room temperature indicates that exciton polarization dominates.

Finally, in order to provide insight into variations of the optically initialized valley polarizations over large areas, we spatially resolved the dynamics of valley states in monolayer MoS_2. Since recent PL spatial mapping [39,40] and second-harmonic generation imaging [41] have been able to identify the crystal orientation and edge morphology of CVD-grown MoS_2 monolayers, it is important to explore the valley excitonic properties near the edges and grain boundaries of TMDC monolayer flakes. This spatial mapping was achieved by moving the cryostat and sample in the x-y plane [shown in Fig. 1(a)] while maintaining the spatial overlap of the pump and probe beams ($\sim$1.5-μm-diameter spot size). We performed a one-dimensional (1D) scan of the temporal evolution of the TRKR traces across a monolayer MoS_2 flake, as shown in Supplemental Material Fig. S4 [24]. Taking into account the stability of our setup and the time needed, we were not able to perform such spatial mapping of TRKR traces in 2D. However, the 1D scan did not show any significant spatial variations in the decay dynamics across the flake. Thus, in this work, we will mainly focus on the spatial variation of the TRKR intensity at a fixed pump-probe delay time.

Figure 5 shows the spatial distributions of the TRKR intensity at a fixed pump-probe delay time ($\Delta t = 0.5$ ps) for six different MoS_2 monolayer flakes along with their corresponding optical microscopy images, at both low temperature ($T = 10$ K) and room temperature. The TRKR intensities were normalized for each sample. Because exciton depolarization dominates the decay dynamics during the initial several picoseconds as discussed above, the Kerr rotation intensity at $\Delta t = 0.5$ ps is mostly an indication of the valley exciton polarization. Although each flake had slightly different spatial dependence on the optically initialized valley polarization, higher TRKR intensities were generally observed near the center of the flakes. As opposed to the second-harmonic

optical imaging [41], the edge states in monolayer MoS_2 did not reveal any enhanced valley exciton polarization in our 2D spatial maps. The isolated star-like and triangular-shape flakes are formed during the CVD growth process with complex polycrystalline structures [39]. The resulting grain boundaries have been demonstrated from previous reports to quench excitons [39,40,42]. Similar 2D spatial maps of PL intensities were obtained from three different MoS_2 monolayers as shown in Supplemental Material Fig. S5 [24]. Thus, these grain boundaries are likely to have led to the reduced valley exciton polarizations near the edges as observed from the TRKR spatial maps here. Alternatively, the observed weaker TRKR intensities near the edges could be associated with an energetically disordered edge region that may form during the termination growth process, such as that resulting from lattice orientation mismatch and nonbonding second-layer growth [43]. This edge region is expected to be more complicated than a particular atomic termination such as a Mo- or S-zigzag termination, and it may cause largely quenched valley polarization compared to the interior, locally ordered region [44]. Additionally, owing to the large exciton binding energy of monolayer MoS_2, the spatially resolved valley dynamics measured by TRKR could even be detected at room temperature, as shown in Fig. 5(d)–5(f). Figure S6 in the Supplemental Material [24] shows the spatially resolved valley dynamics of additional monolayer MoS_2 and WSe_2 samples.

In conclusion, our results reveal the ultrafast valley dynamics of exciton, trion, and defect-related localized states in monolayer MoS_2 and WSe_2 using TRKR measurements with sub-picosecond temporal resolution. Excitation wavelength-dependent TRKR measurements revealed the origin of the observed Kerr rotation in monolayer MoS_2, which is induced by the imbalance between the populations in the $\pm K$ valleys upon optical excitation and is linearly proportional to the valley polarization in the material. A maximum TRKR intensity was observed when the excitation was tuned slightly above the *A* exciton resonance, indicating the largest optically initialized valley polarization. Different temperature dependencies of the valley dynamics between monolayer MoS_2 and WSe_2 revealed distinct underlying mechanisms for the slow decay components. Furthermore, the spatially resolved TRKR measurements revealed weaker valley polarizations near the edges of the MoS_2 monolayer flakes, which is interpreted to be associated with quenched excitons near the grain boundaries or a disordered edge region of CVD-grown monolayer MoS_2. We also observed TRKR for both monolayer MoS_2 and WSe_2 at room temperature, which may open the possibility for valleytronic devices operating at ambient conditions. Moreover, our TRKR measurements and results are not unique to MoS_2 and WSe_2. Similar measurements can be directly extended to other direct bandgap 2D materials, such as $MoSe_2$ and WS_2, to investigate the valley dynamics in different materials. These temporal and spatial TRKR experiments elucidate pathways to manipulate multiple excitonic states in monolayer TMDCs, which may also lead to the design of hybrid structures composed of different low-dimensional materials, which are promising for future integrated on-chip nanoscale components [45–47].

J.H., T.B.H, and M.H.M. acknowledge support from the Air Force Office of Scientific Research Young Investigator Research Program (AFOSR, Grant. No. FA9550-15-1-0301). This research was supported as part of the Center for Excitonics, an Energy Frontier Research Center funded by the U.S. Department of Energy, Office of Science, Basic Energy Sciences (BES), under award number DE-SC0001088. T.M. and J.K. acknowledge support from DOE BES Grant No. DESC0001088.

[1] Q. H. Wang, K. Kalantar-Zadeh, A. Kis, J. N. Coleman, and M. S. Strano, Nat. Nanotechnol. **7**, 699 (2012).
[2] K. F. Mak, C. Lee, J. Hone, J. Shan, and T. F. Heinz, Phys. Rev. Lett. **105**, 136805 (2010).
[3] D. Xiao, G. B. Liu, W. X. Feng, X. D. Xu, and W. Yao, Phys. Rev. Lett. **108**, 196802 (2012).
[4] K. F. Mak, K. L. He, J. Shan, and T. F. Heinz, Nat. Nanotechnol. **7**, 494 (2012).
[5] H. Zeng, J. Dai, W. Yao, D. Xiao, and X. Cui, Nat. Nanotechnol. **7**, 490 (2012).
[6] G. Aivazian, Z. Gong, A. M. Jones, R. L. Chu, J. Yan, D. G. Mandrus, C. Zhang, D. Cobden, W. Yao, and X. D. Xu, Nat. Phys. **11**, 148 (2015).
[7] J. S. Ross, S. Wu, H. Yu, N. J. Ghimire, A. M. Jones, G. Aivazian, J. Yan, D. G. Mandrus, D. Xiao, W. Yao, and X. Xu, Nat. Commun. **4**, 1474 (2013).
[8] D. Lagarde, L. Bouet, X. Marie, C. R. Zhu, B. L. Liu, T. Amand, P. H. Tan, and B. Urbaszek, Phys. Rev. Lett. **112**, 047401 (2014).
[9] G. Wang, L. Bouet, D. Lagarde, M. Vidal, A. Balocchi, T. Amand, X. Marie, and B. Urbaszek, Phys. Rev. B **90**, 075413 (2014).
[10] T. Yan, X. Qiao, X. Liu, P. Tan, and X. Zhang, Appl. Phys. Lett. **105**, 101901 (2014).
[11] T. Korn, S. Heydrich, M. Hirmer, J. Schmutzler, and C. Schüller, Appl. Phys. Lett. **99**, 102109 (2011).
[12] C. Robert, D. Lagarde, F. Cadiz, G. Wang, B. Lassagne, T. Amand, A. Balocchi, P. Renucci, S. Tongay, B. Urbaszek, and X. Marie, Phys. Rev. B **93**, 205423 (2016).
[13] C. Poellmann, P. Steinleitner, U. Leierseder, P. Nagler, G. Plechinger, M. Porer, R. Bratschitsch, C. Schüller, T. Korn, and R. Huber, Nat. Mater. **14**, 889 (2015).
[14] H. Wang, C. Zhang, and F. Rana, Nano Lett. **15**, 339 (2015).
[15] H. Shi, R. Yan, S. Bertolazzi, J. Brivio, B. Gao, A. Kis, D. Jena, H. G. Xing, and L. Huang, ACS Nano **7**, 1072 (2013).
[16] C. Mai, A. Barrette, Y. Yu, Y. G. Semenov, K. W. Kim, L. Cao, and K. Gundogdu, Nano Lett. **14**, 202 (2014).
[17] W.-T. Hsu, Y.-L. Chen, C.-H. Chen, P.-S. Liu, T.-H. Hou, L.-J. Li, and W.-H. Chang, Nat. Commun. **6**, 8963 (2015).
[18] L. Yang, N. A. Sinitsyn, W. Chen, J. Yuan, J. Zhang, J. Lou, and S. A. Crooker, Nat. Phys. **11**, 830 (2015).
[19] L. Yang, W. Chen, K. M. McCreary, B. T. Jonker, J. Lou, and S. A. Crooker, Nano Lett. **15**, 8250 (2015).
[20] M. H. Mikkelsen, J. Berezovsky, N. G. Stoltz, L. A. Coldren, and D. D. Awschalom, Nat. Phys. **3**, 770 (2007).
[21] J. Berezovsky, M. H. Mikkelsen, N. G. Stoltz, L. A. Coldren, and D. D. Awschalom, Science **320**, 349 (2008).

[22] B. M. Norman, C. J. Trowbridge, D. D. Awschalom, and V. Sih, Phys. Rev. Lett. **112**, 056601 (2014).
[23] X. Ling, Y.-H. Lee, Y. Lin, W. Fang, L. Yu, M. S. Dresselhaus, and J. Kong, Nano Lett. **14**, 464 (2014).
[24] See Supplemental Material at http://link.aps.org/supplemental/10.1103/PhysRevB.95.075428 details about the PL, Raman, and atomic-force microscopy characterizations of the mechanically exfoliated WSe_2 monolayers, excitation power-dependent TRKR measurements for a monolayer MoS_2 flake, sample variations of the extracted decay components from 20 different monolayer MoS_2 flakes, spatial variation of the temporal evolution of valley dynamics in 1D, spatial dependence of the PL intensity, and additional spatial dependence of the TRKR intensity at a fixed pump-probe delay time from monolayer MoS_2 and WSe_2 flakes, as well as a table of some of the published time-resolved and pump-probe measurements.
[25] J. Lee, K. F. Mak, and J. Shan, Nat. Nanotechnol. **11**, 421 (2016).
[26] I. A. Yugova, M. M. Glazov, E. L. Ivchenko, and A. L. Efros, Phys. Rev. B **80**, 104436 (2009).
[27] M. M. Glazov, Phys. Solid State **54**, 1 (2012).
[28] G. M. Akselrod, T. Ming, C. Argyropoulos, T. B. Hoang, Y. Lin, X. Ling, D. R. Smith, J. Kong, and M. H. Mikkelsen, Nano Lett. **15**, 3578 (2015).
[29] J. Huang, T. B. Hoang, and M. H. Mikkelsen, Sci. Rep. **6**, 22414 (2016).
[30] C. R. Zhu, K. Zhang, M. Glazov, B. Urbaszek, T. Amand, Z. W. Ji, B. L. Liu, and X. Marie, Phys. Rev. B **90**, 161302(R) (2014).
[31] T. Yu and M. W. Wu, Phys. Rev. B **89**, 205303 (2014).
[32] M. M. Glazov, T. Amand, X. Marie, D. Lagarde, L. Bouet, and B. Urbaszek, Phys. Rev. B **89**, 201302(R) (2014).
[33] X.-X. Zhang, Y. You, S. Y. F. Zhao, and T. F. Heinz, Phys. Rev. Lett. **115**, 257403 (2015).
[34] G. Plechinger, P. Nagler, A. Arora, R. Schmidt, A. Chernikov, A. G. del Águila, P. C. M. Christianen, R. Bratschitsch, C. Schüller, and T. Korn, Nat. Commun. **7**, 12715 (2016).
[35] A. A. Mitioglu, L. Klopotowski, D. K. Maude, G. Deligeorgis, S. Anghel, L. Kulyuk, and P. Plochocka, arXiv:1507.00496 (2015).
[36] A. M. Jones, H. Yu, N. J. Ghimire, S. Wu, G. Aivazian, J. S. Ross, B. Zhao, J. Yan, D. G. Mandrus, D. Xiao, W. Yao, and X. D. Xu, Nat. Nanotechnol. **8**, 634 (2013).
[37] K. He, N. Kumar, L. Zhao, Z. Wang, K. F. Mak, H. Zhao, and J. Shan, Phys. Rev. Lett. **113**, 026803 (2014).
[38] K. F. Mak, K. L. He, C. Lee, G. H. Lee, J. Hone, T. F. Heinz, and J. Shan, Nat. Mater. **12**, 207 (2013).
[39] A. M. van der Zande, P. Y. Huang, D. A. Chenet, T. C. Berkelbach, Y. You, G.-H. Lee, T. F. Heinz, D. R. Reichman, D. A. Muller, and J. C. Hone, Nat. Mater. **12**, 554 (2013).
[40] Z. Liu, M. Amani, S. Najmaei, Q. Xu, X. Zou, W. Zhou, T. Yu, C. Qiu, A. G. Birdwell, F. J. Crowne, R. Vajtai, B. I. Yakobson, Z. Xia, M. Dubey, P. M. Ajayan, and J. Lou, Nat. Commun. **5**, 5246 (2014).
[41] X. Yin, Z. Ye, D. A Chenet, Y. Ye, K. O'Brien, J. C. Hone, and X. Zhang, Science **344**, 488 (2014).
[42] S. Wang, Y. Rong, Y. Fan, M. Pacios, H. Bhaskaran, K. He, and J. H. Warner, Chem. Mater. **26**, 6371 (2014).
[43] W. Bao, N. J. Borys, C. Ko, J. Suh, W. Fan, A. Thron, Y. Zhang, A. Buyanin, J. Zhang, S. Cabrini, P. D. Ashby, A. Weber-Bargioni, S. Tongay, S. Aloni, D. F. Ogletree, J. Wu, M. B. Salmeron, and P. J. Schuck, Nat. Commun. **6**, 7993 (2015).
[44] S. Najmaei, Z. Liu, W. Zhou, X. Zou, G. Shi, S. Lei, B. I. Yakobson, J.-C. Idrobo, P. M. Ajayan, and J. Lou, Nat. Mater. **12**, 754 (2013).
[45] J. D. Caldwell, I. Vurgaftman, J. G. Tischler, O. J. Glembocki, J. C. Owrutsky, and T. L. Reinecke, Nat. Nanotechnol. **11**, 9 (2016).
[46] M. Liu, X. Yin, E. Ulin-Avila, B. Geng, T. Zentgraf, L. Ju, F. Wang, and X. Zhang, Nature **474**, 64 (2011).
[47] Z. Fei, A. S. Rodin, G. O. Andreev, W. Bao, A. S. McLeod, M. Wagner, L. M. Zhang, Z. Zhao, M. Thiemens, G. Dominguez, M. M. Fogler, A. H. C. Neto, C. N. Lau, F. Keilmann, and D. N. Basov, Nature **487**, 82 (2012).